

Flaring Latitudes in Ensembles of Low Mass Stars

Ekaterina Ilin,¹★ Ruth Angus,^{2,3} Rodrigo Luger,³ Brett M. Morris,⁴ Florian U. Jehn,^{5,6}

¹*Leibniz Institute for Astrophysics Potsdam (AIP), An der Sternwarte 16, 14482 Potsdam, Germany*

²*Department of Astrophysics, American Museum of Natural History, 200 Central Park West New York, NY 10024, USA*

³*Center for Computational Astrophysics, 162 5th Ave., New York, NY 10010, USA*

⁴*Space Telescope Science Institute, Baltimore, MD 21218, USA*

⁵*Institute for Landscape Ecology and Resources Management (ILR),*

Research Centre for BioSystems, Land Use and Nutrition (iFZ),

Justus Liebig University Giessen, Heinrich-Buff-Ring 26, 35390 Giessen, Germany

⁶*Alliance to Feed the Earth in Disasters (ALLFED), Fairbanks, AK, USA.*

Accepted 2023 May 31. Received 2023 May 30; in original form 2022 December 21

ABSTRACT

The distribution of small-scale magnetic fields in stellar photospheres is an important ingredient in our understanding of the magnetism of low mass stars. Their spatial distribution connects the field generated in the stellar interior with the outer corona and the large scale field, and thereby affects the space weather of planets. Unfortunately, we lack techniques that can locate them on most low-mass stars. One strategy is to localize field concentrations using the flares that occur in their vicinity.

We explore a new method that adapts the spot simulation software `fleck` to study the modulation of flaring times as a function of active latitude. We use empirical relations to construct flare light curves similar to those available from Kepler and the Transiting Exoplanet Survey Satellite (TESS), search them for flares, and use the waiting times between flares to determine the location of active latitudes.

We find that the mean and standard deviation of the waiting time distribution provide a unique diagnostic of flaring latitudes as a function of the number of active regions. Latitudes are best recovered when stars have three or less active regions that flare repeatedly, and active latitude widths below 20 deg; when either increases, the information about the active latitude location is gradually lost. We demonstrate our technique on a sample of flaring G dwarfs observed with the Kepler satellite, and furthermore suggest that combining ensemble methods for spots and flares could overcome the limitations of each individual technique for the localization of surface magnetic fields.

Key words: stars: magnetic field – stars: flare – methods: statistical

1 INTRODUCTION

The presence and location of active latitudes – belts of strong, small-scale surface magnetic fields, and elevated stellar activity – is poorly known on stars other than the Sun (Berdyugina 2005; Hathaway 2015). Disk-integrated observations that measure stellar activity of the star as a whole, e.g., chromospheric and coronal emission, spot-induced variability, and flares, have provided crucial constraints on how stars produce magnetic fields (Kővári & Oláh 2014), and their impact on habitability (Airapetian et al. 2020). However, to further advance these fields, spatially resolved information about various stellar activity phenomena – like active latitudes of starspots and flares – is required, yet largely missing.

1.1 Stellar dynamo

The amplification of magnetic fields inside the Sun, a process known as solar dynamo, is driven by the movement of hot plasma in the

convection zone, and forces introduced by stellar differential rotation (Parker 1955). Once the field is amplified, it emerges through the surface, forming complex magnetic loop structures. Their footpoints form active regions and sunspots in a range of low latitudes, which vary throughout the solar cycle to form the famous butterfly diagram (Hathaway 2015). The stellar counterparts of these spots and flares can be large enough to be detected in disk-integrated observations. We observe them as modulations of the total stellar brightness periodic with stellar rotation, or sudden brightenings during flares (e.g. Notsu et al. 2013).

In low mass stars, the exact mechanism behind the stellar dynamo is under active debate (Brun & Browning 2017). The interior of a star can be measured using stellar oscillations, but asteroseismology is currently limited to bright solar-type and giant stars (García & Ballot 2019; Rodríguez-López 2019), so that observers have to mostly rely on indicators from the exterior. One way to discriminate between different models is to map where magnetic fields emerge from the stellar interior to the surface (Fan 2009; Bice & Toomre 2022; Weber & Browning 2016). The locations of these dynamic fields are pinpointed by stellar flares, magnetically driven explosions in the corona that heat the footpoints to emit thermally at $\sim 10,000$ K (Kowalski

★ E-mail: eilin@aip.de

et al. 2013), which can be found in all stars with an outer convection zone (Davenport 2016; Günther et al. 2020; Howard et al. 2019). Flaring latitudes are of particular interest because they are direct evidence of dynamic and strong small-scale surface fields, a marker of field emergence (Benz & Güdel 2010). For example, while old Sun-like stars are expected to show low latitude active regions (Fan 2009), models suggest that in young rapidly rotating stars they should arise closer to the poles (Schuessler & Solanki 1992; Yadav et al. 2015; Weber & Browning 2016). Moreover, active latitudes shift over the course of the solar cycle, another distinct feature of the dynamo operating within, which is suggested in other stars as well (Nielsen et al. 2019).

1.2 Space weather

When flares are accompanied by particle eruptions with a preferred direction, such as coronal mass ejections (CME) and energetic particle events, their launch site influences whether a planet in the orbit will be hit or missed by the blast. If the planet is hit by a fast cloud of energetic and magnetized plasma, the planet can experience both temporary and permanent changes in its atmospheric chemistry (Tilley et al. 2019; Chen et al. 2021; Chadney et al. 2017), as well as increased atmospheric escape (Hazra et al. 2022). If the magnetic activity is as high as in many of the cool stars observed to date, the planet may even suffer a partial or complete loss of its envelope over time (Khodachenko et al. 2007; Lammer et al. 2007; Cherenkov et al. 2017). Therefore, tracing flaring latitudes could explain variability in exoplanet atmosphere characteristics, such as, for instance, conjured for HD 189733 b. Its atmospheric hydrogen appears to be escaping at lower rates before a flare was observed in X-ray compared to afterward (Lecavelier des Etangs et al. 2012). If this is the case, the associated particles likely erupted from a latitude near the planet’s orbital plane.

1.3 Exoplanet characterization

Even if the effects of latitude-dependent stellar activity are moderate for the planet, the presence of active latitudes indirectly complicates its characterization. The emission from a stellar surface with active latitudes is inhomogeneous. If it is then falsely assumed to be uniform, the depth of a transiting planet may be measured against a biased baseline that is brighter or darker than the average surface, and falsely yield a too large or too small radius for the planet (Morris et al. 2018a). Furthermore, the presence of active regions in or out of the passageway of transiting planets can distort atmospheric signal in transmission spectra (McCullough et al. 2014; Rackham et al. 2018; Cauley et al. 2017, 2018), and interfere with the orbital radial velocity signal (Huber et al. 2009; Meunier & Lagrange 2019; Meunier et al. 2019). For example, the characterization of the seven planets surrounding TRAPPIST-1 may be affected by an active latitude of bright spots associated with flaring activity outside their transit chords (Morris et al. 2018b; Ducrot et al. 2018). Without a solid understanding of the spatial distribution of active regions on the surfaces of exoplanet hosts, access to the planets’ atmospheres will remain limited.

1.4 Measuring active latitudes

On the Sun, flares and spots occur in a belt below about 30 deg latitude around the equator (Chen et al. 2011). On other stars, we know comparably little. Active latitudes have been measured in a number

of ways, including spot occultations by misaligned planets (Morris et al. 2017; Netto & Valio 2020), asteroseismology (Thomas et al. 2019; Bazot et al. 2018), light curve inversions of stars with rotational modulation by spots (Huber et al. 2010; Santos et al. 2017; Basri et al. 2022), and, albeit with low spatial resolution, using spectropolarimetry (Unruh et al. 1995; Perugini et al. 2021). Some of the handful of stars investigated in these works appear active, with spots located close to the poles or preferably near the equator. Others show spots at multiple distinct latitudes, or in a broad range, but the sample is too small to confidently identify meaningful trends.

Localizing flaring latitudes is particularly challenging. They occur randomly in time, limiting time-resolved spectroscopic methods to the most actively flaring nearby stars, such as BO Mic (Wolter et al. 2008). Except for the Sun, we lack the observations to tell if and how they are spatially related to spots, which would otherwise simplify the task. Stellar flare locations have only been captured serendipitously (e.g. Wolter et al. 2008; Schmitt & Favata 1999), or for exceptionally energetic events on particularly rapidly rotating stars (Ilin et al. 2021a). For the bulk of flaring stars, however, localization methods are missing.

This work explores a method that allows us to systematically infer the flaring latitudes in ensembles of a wide range of stars using photometric observations, such as currently available from the Kepler (Koch et al. 2010) and Transiting Exoplanet Survey Satellite (TESS, Ricker et al. 2015) missions. In Section 2, we present our simulations of flaring light curves on stars with active latitudes. In Section 3, we use these synthetic light curves to show how we can use the occurrence times of flares to recover the location of an active latitude, and apply the method to a sample of flaring G dwarf stars in Kepler. We discuss the advantages and limitations of this approach in Section 4, and summarize in Section 5.

2 METHODS

We simulate ensembles of flaring stars to explore if information about the latitudinal distribution of flaring regions can be inferred from the waiting time distributions of flares in stellar ensembles.

2.1 Waiting time and night length

We define **waiting time** as the time between two subsequent flares phase folded with stellar rotation. That is, waiting time is measured in units of rotational phase, not days, allowing us to build ensembles from stars with varying rotation periods. In other words, we measure the flare phases, sort them ascending, and calculate the waiting times from the resulting series of timestamps.

A flaring region viewed equator-on, i.e. with stellar inclination $i = 90^\circ$, will be seen flaring 50% of the time, and will be hidden behind the limb for the other 50%. In contrast, a flaring region close to the rotational pole with $i = 0^\circ$ is seen 100% of the time. At all other inclinations, the night length will vary with the latitude of the active region (Fig. 1). Here, **night length** is defined as the time during which a flaring region is hidden from the observer, given its latitude and the star’s inclination. For an ensemble of stars with random orientations, we observe a distribution of night lengths with a characteristic mean and standard deviation. We can trace the night length through the timing of flares that occur in the active latitude, which allows us to infer its location. As our results will show, the picture is somewhat more complicated, which we address in Section 3.4.

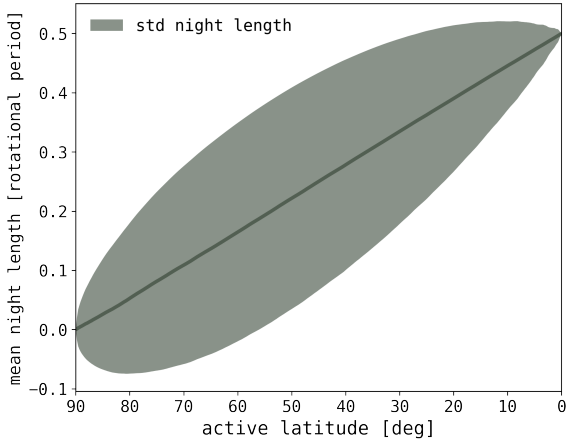


Figure 1. Mean and standard deviation of night lengths in an ensemble of randomly oriented stars. We define night length as the time during which a flaring region is hidden from the observer as the star rotates. If the active latitude is positioned either at the pole or the equator, the orientation does not affect the night length. Otherwise, night lengths vary with inclination (grey shaded area).

2.2 Marginalizing over inclination

For the stars in the ensemble we do not know the inclination i which, for any individual star, creates a degeneracy in the latitude of a particular flaring region. However, we can assume that the stars’ rotation axes are oriented randomly, so that we can marginalize over i . If the flaring regions in the ensemble are located at approximately the same latitude, the night lengths and therefore the waiting times of the ensemble will have a distribution characteristic of that latitude.

2.3 Ensembles of flaring stars

We simulate light curves of ensembles of flaring stars with different active latitudes, and apply standard flare finding techniques to identify flare peak times, i.e., iteratively clipping positive outliers from a rolling median in the light curve to find the quiescent flux level, and then identifying series of outliers from this quiescent level as flare candidates. We then calculate the waiting time distribution, and use the mean μ and standard deviation σ of the distribution to characterize it as a function of active latitude. In the simple case of a well-localized flaring region at a fixed active latitude θ , we construct the ensemble as follows:

For each star, we define a flaring region, assuming that it is stable. Stable means that in the course of observation, the region has already fully emerged, does not decay, and produces flares randomly, following a Poisson process in time at a defined rate. In the application to real observations, the varying lifetimes of spots and active regions need to be taken into account (see Sections 3.5 and 4.3).

2.4 Individual flares

To create a realistic individual flare, we invert the Davenport et al. (2014) flare template parametrization with variable full width at half the maximum flux ($t_{1/2}$) and amplitude (a). We infer a from the empirical relation between amplitude and equivalent duration ED using a sample of ultracool dwarfs (Fig. 2). The equivalent duration ED is the time the star needs to emit as much light as the flare did (Gershberg 1972), which is a relative unit for the flare energy.

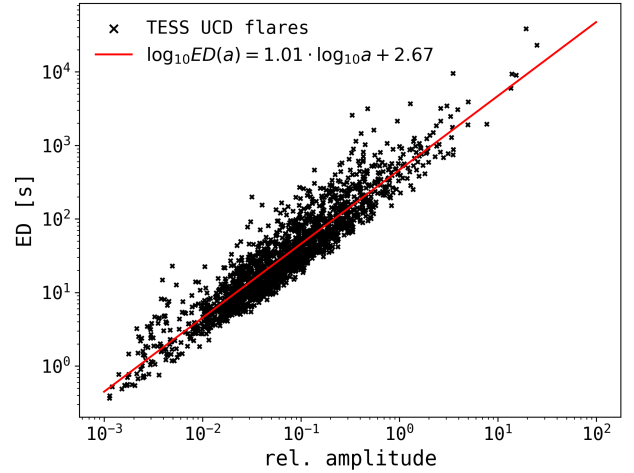


Figure 2. The relation between equivalent duration ED and relative amplitude of flares (black dots) in ultra-cool dwarfs (spectral type M6-M9) observed by TESS (Pineda et al. in prep.). The red line is the power law fit used to infer relative amplitude a from ED (see Section 2.4).

With given ED , we infer a , and then use the parametrization from Davenport et al. (2014) to calculate $t_{1/2}$.

2.5 Flare frequency distributions

Since flares are distributed on a power law across a wide range of energies E (or ED) and stellar properties (Shibayama et al. 2013; Maehara et al. 2015; Ilin et al. 2021b), we create a number N of flares based on flare rate β , drawn from an energy distribution with power law slope α :

$$N(E) = \beta \cdot E^{-\alpha} \quad (1)$$

In our simulations, the distribution of flare energies in each flaring region follows a power law with slope α between 1.5 and 2.5, and a rate β between 1 and 60.

2.6 Flare injection, rotational modulation, and recovery

We then distribute the flares with their respective a and $t_{1/2}$ in a light curve according to a Poisson process (grey curve in Fig. 3). We chose the light curve cadence and Gaussian noise such that all injected flares are recovered in the unmodulated light curve. That means that all flares have their peaks 3σ above the noise level for at least three consecutive data points. Next, we assign a latitude θ and arbitrary longitude ϕ , pick a random orientation of the star (random in $\cos i$). We use `fleck`, a software package for simulating rotational modulation of stars due to starspots (Morris 2020a,b) to rotate the flaring stars, replacing the dark spots with flaring regions. In other words, in `fleck`, we replace the constant darkening caused by a spot with the time-varying brightening caused by a flare. We fix the flaring region area at $\sim 10^{-4}$ of the stellar hemisphere area, or equivalently 1% of the stellar radius, which is within the $10^{-5} - 10^{-3}$ range of estimated areas of the white light footpoints of energetic solar and stellar flares (Metcalf et al. 2003; Kowalski et al. 2010, 2013). For completeness, we applied quadratic limb darkening. This only marginally affects the flare amplitude compared to geometric

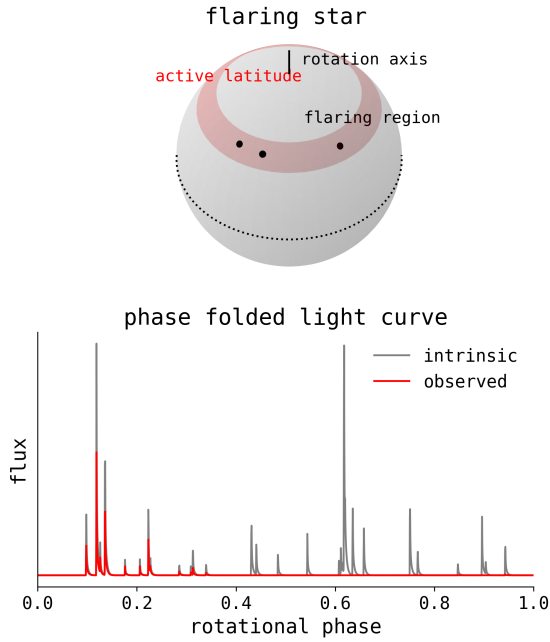


Figure 3. Model illustration: Star with flaring active latitudes. Top: stellar sphere with three active regions placed within an active latitude strip. Bottom, grey line: Phase folded light curve of a single active region, assuming other variability signatures have been completely removed. Bottom, red: Same light curve but as seen by the observer, accounting for geometric foreshortening and visibility, as the star rotates. As a consequence, some flares appear lower in amplitude, while others are not detected at all (see Section 2.6).

foreshortening, assuming that the flare emission is optically thick (see Fig. B1 in Ilin et al. 2021a).

We do not apply spot induced rotational modulation to the light curve, assuming that it was removed successfully while preserving the flare signal, for which various algorithms exist (e.g. Shibayama et al. 2013; Van Doorselaere et al. 2017; Raetz et al. 2020; Ilin et al. 2021b). These algorithms can distinguish rotational modulation from flares as long as the time scales are sufficiently different for both. This is true even for the most rapidly rotating stars with periods below 10 h, where very long duration flares can occur, but are very rare (Ilin et al. 2021a). Those events are easily identified as flares by eye due to their large amplitudes. Flares that are shorter, but still evolve more gradually than typical fast-rise-exponential-decay flares (see Fig. 3) may be lost while removing rotational modulation. But for those, the distinction between flares and other sources of variability like spots or faculae becomes increasingly uncertain, so it is not clear if missing these "flares" is an actual loss.

After rotating the star, a fraction of flares is no longer detected with AltaiPony because it occurs on the back of the star, or close to the limb, so that the amplitude falls below the noise level (red curve in Fig. 3). We only use these detected flares to calculate the waiting times.

2.7 Ensembles of stars with different active latitudes

We repeat the above steps 200 times for each choice of latitude θ . This creates an ensemble of 200 flaring light curves on stars with random orientations, random flare times, picking α randomly from 1.5 to 2.5, choosing random flaring rates β . All stars share the same flaring latitude with the same width ($\Delta\theta = 5$ deg). From simulation to

Table 1. Model parameters.

parameter	values
flare rate β	1-60 flares per light curve
energy distribution power law slope α^*	1.5 – 2.5
number of flaring regions per star	1-5
active latitude center θ	5-85 deg
active latitude width $\Delta\theta$	5-40 deg
active longitude ϕ	0-360 deg random
flaring region size	10^{-4} stellar hemisphere
quadratic limb darkening coefficients	0.5079, 0.2239
stars in ensemble	200
* per active region	

simulation, we vary the average β in the ensembles so that our results cover different mean waiting times μ (see Fig. 4). We note that we do not need to specify the number of rotation periods covered by each light curve, because we only require phase-folded light curves to measure the waiting times. At a fixed flare rate, more rotations mean more flares in the total light curve, which we can control by setting β directly.

The number of 200 stars in the sample is motivated, on the one hand, by the requirement that we need a sufficient number of stars to marginalize over inclination. On the other hand, we wanted to demonstrate our technique on a realistic number of flaring stars with similar properties, and therefore, expectedly similar flaring latitudes (see Section 4 for a discussion of relevant criteria in the sample selection). This can be achieved, for instance, with the growing archive of space based light curves of flaring stars (see, e.g., Davenport 2016; Günther et al. 2020; Yang et al. 2017; Feinstein et al. 2020).

We list the studied ranges for α , β , and further parameters in Table 1.

3 RESULTS

Based on the results of our simulations, we calibrate quadratic relations between θ and the mean and standard deviation of waiting times, for different numbers of flares and different hemispheric configurations. The only additional information needed about the stars is their rotational period. This process is outlined in more detail in Section 3.1.

We can use the waiting times between flares to locate the active latitude on the stellar surface if an actively flaring latitude is present in an ensemble of stars. Our results present a straightforward way to check whether the waiting time distribution of flares is informative in a given ensemble, and to find out what it can tell us about the presence, number and location of active latitudes. Our simulations were chosen to represent the currently available sample sizes achievable with light curves from the Kepler and TESS archives. While compiling a sufficiently large data set is outside the scope of this paper, in Section 3.5, we demonstrate how our technique can be applied using a small sample of flaring G dwarfs observed by Kepler (Okamoto et al. 2021).

3.1 Analytical expression for active latitude inference

In our chosen set of simulations, we picked a $\Delta\theta = 5$ deg wide active latitude, a typical solar value around the activity maximum (Fig. 32 in Hathaway 2015), and explored the cases of either an ensemble of stars with only one active region per star, or 1-3, or 3-5 actively flaring

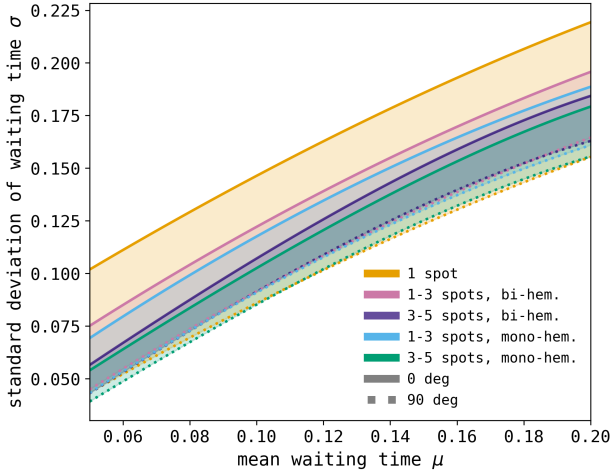


Figure 4. Ranges of active latitudes as a function of μ and σ , calculated from the relations in Table 2. Each line shows the $\theta = 0$ deg (solid) and 90 deg (dotted) margins of the colored latitude range in between. Stellar ensembles with a single low latitude active region occupy a distinct region in the diagram (orange area). Other combinations of μ and σ are ambiguous because two or more ranges overlap.

regions per star. In the case of 1-3 and 3-5 flaring regions, we distinguish the cases where either all flaring regions are on the same hemisphere (mono-hemispheric) or distributed over both hemispheres (bi-hemispheric), at random longitudes, because the night lengths for stars with inclined rotation axes differ for Northern and Southern hemispheres. On the Sun, active regions appear on both hemispheres. However, this is poorly constrained on other stars. In magnetohydrodynamical simulations of fully convective M dwarfs, flux emergence can potentially be both mono- and bi-hemispheric (Browning 2008; Brown et al. 2020; Käpylä 2021). We therefore simulate light curves for eight runs of 100,000 light curves each for each of the five setups (1, 1-3 mono-hem., 1-3 bi-hem., 3-5 mono-hem., 3-5 bi-hem.). The eight runs differ by the number of flares chosen for each active region, which translates into a range of detected flaring rates. We then split the sample into ensembles of 200 stars with the same active latitude θ and calculate μ and σ for the ensemble, taking 5 deg steps in latitude, and ignoring the equator and the pole, i.e., [5, 10, ..., 85] deg. We fit a polynomial expression,

$$\theta = a_1 \cdot \mu^2 + a_2 \cdot \mu + b_1 \cdot \sigma^2 + b_2 \cdot \sigma + c, \quad (2)$$

to the resulting (eight runs) \times (17 latitudes) = 136 data points in each setup. The best-fit parameters are given in Table 2.

The range of resulting μ and σ values in our synthetic data is shown in Fig. 4. The colored areas contain the measured combinations of μ and σ for each setup. That means, if a combination of μ and σ measured in real observations falls outside the colored areas, one or more of the assumptions of the simulation must be violated, e.g., the assumption that flares are generated randomly in time in any given flaring region (see Section 2.6, and the discussion in Section 4.1).

We validated the fitting results using additional simulations of stellar ensembles that were not used for the fit. Figs. 5 and 6 show the residuals when using the best-fit parameters in Table 2 to infer θ in the 1-spot and the bi-hemispheric 1-3 spot cases, respectively. The fewer active regions, the better the recovery of flaring latitudes, if the number of active regions is known. As expected, the uncertainty in the

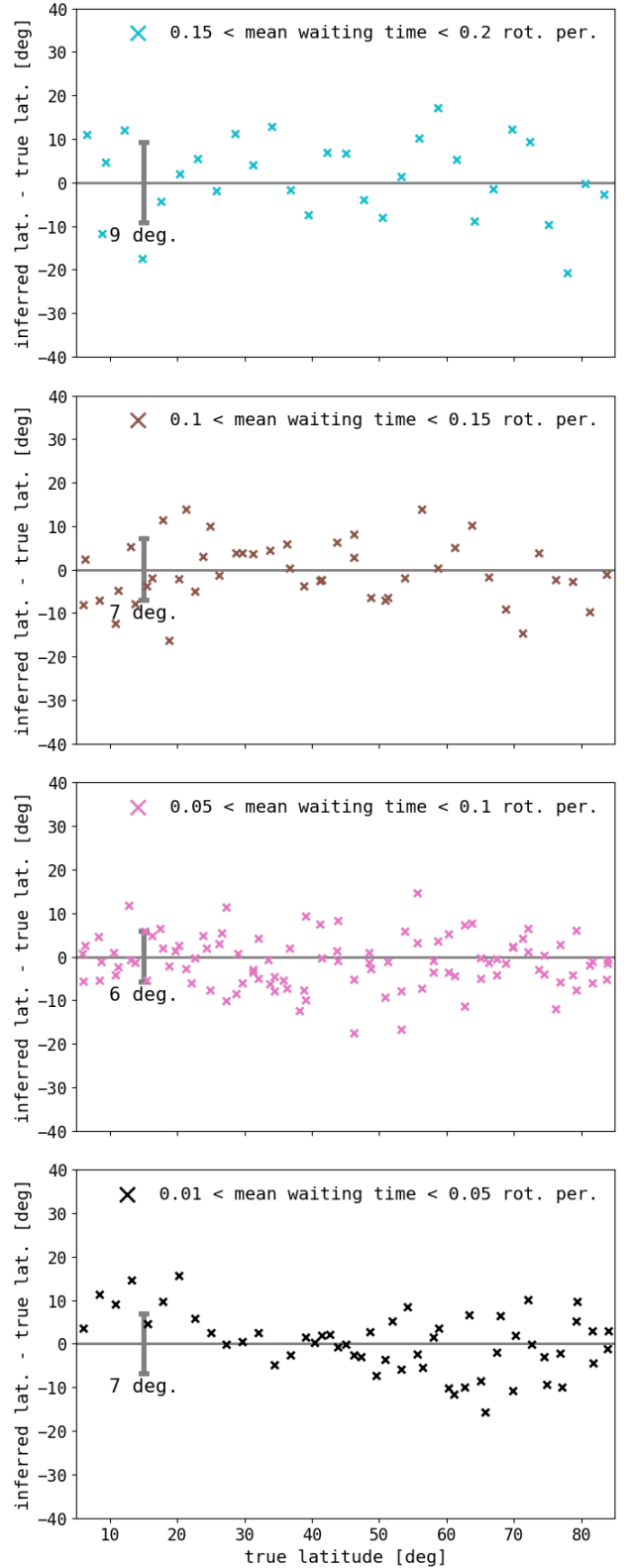


Figure 5. Residuals of inferred latitudes as a function of true latitude. Each data point represents a set of 200 stars with one flaring region placed randomly on either hemisphere, but in the same latitude range for all stars. The residuals decrease with increasing flare rate, i.e., lower μ . The top panel shows the subset with the lowest flaring rate, the bottom panel shows that with the highest flaring rate. To the left in each panel, we show the standard deviation in the residuals.

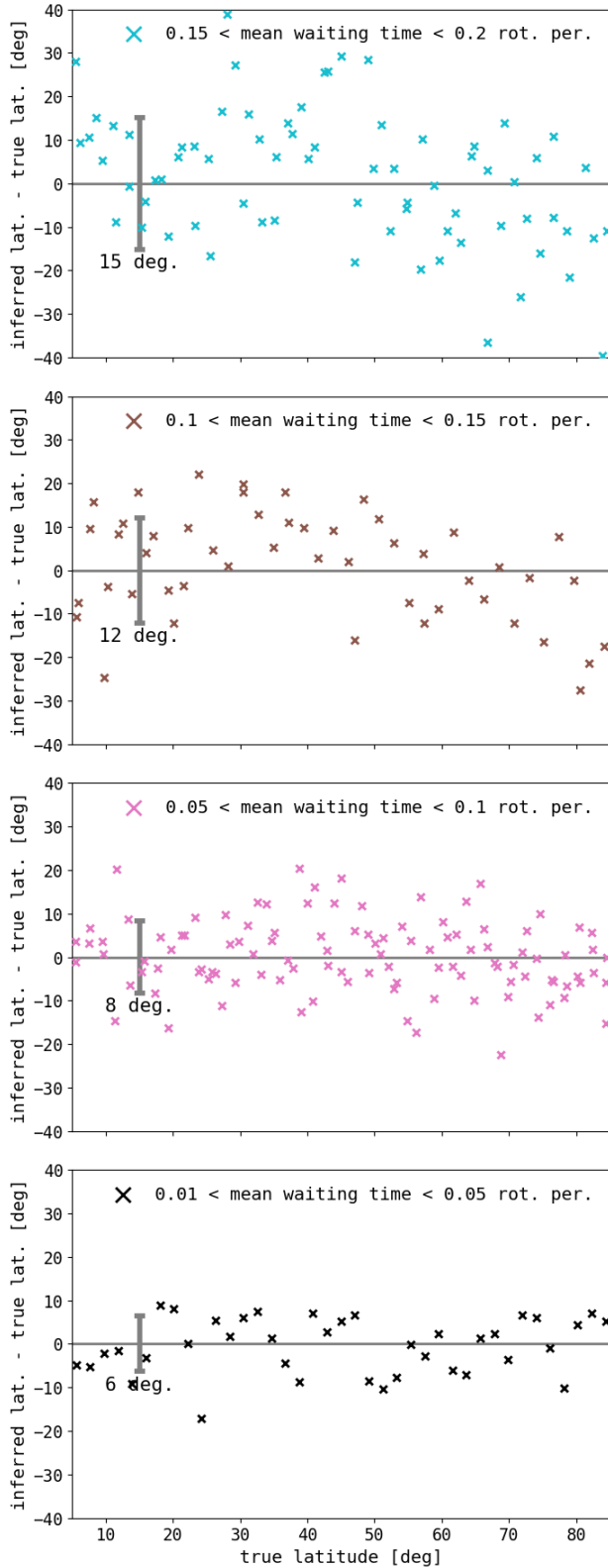


Figure 6. Same as Fig. 5, but for 200-star ensembles with 1-3 flaring regions distributed on both hemispheres.

μ - σ relation for any given active latitude decreases with increasing average flare rate in the ensemble, or, equivalently, shorter mean waiting time μ (to the left in Fig. 4). A shorter mean waiting time can be achieved by increasing the observing baseline per star.

3.2 Flaring region number and hemisphere distribution vs. latitude

For most combinations of the mean μ and standard deviation σ of the waiting time distribution, their interpretation is ambiguous in two ways. Except for single active regions at low latitudes (orange area in Fig. 4), multiple interpretations are usually possible.

First, in the regions where the permitted (μ, σ) areas overlap in Fig. 4, a solution with fewer spots at higher latitudes is degenerate with a solution with more spots at lower latitudes. For example, 1-3 active regions near the equator (solid magenta line in Fig. 4) overlap with the range for a single active region at mid-latitudes.

Second, the wider the active latitude becomes, the more the information on latitude is lost. Fig. 7 shows distributions of μ and σ for four simulations side by side, where only the width of the active latitude $\Delta\theta$ varies between the simulations. For $\Delta\theta \approx 10$ deg and below, the results are completely unaffected, but wider $\Delta\theta \geq 20$ deg increasingly lose the latitudinal information. In the extreme case, where flaring regions are spread over the entire hemisphere ($\Delta\theta = 90$ deg), the waiting time distribution converges on the 45 deg line that roughly bisects each area in Fig. 4 (see also Fig. A1). We also investigated the distinction between mono- and bi-hemispheric distributions of active regions, and found that we cannot distinguish them in our data, so that our latitude inference does not depend on whether there is only one or two active latitudes on opposite hemispheres of the stars.

In practice, given some observed (μ, σ) combination, one can use all available fits in Table 2. Those that return a value between 0 and 90 deg are possible solutions for θ , the remainder can be ruled out. In this way, the latitude inference constrains the latitude of the active region as a function of their number (see Section 3.5 for a demonstration on real observations).

3.3 Flare energies and amplitudes vs. latitude

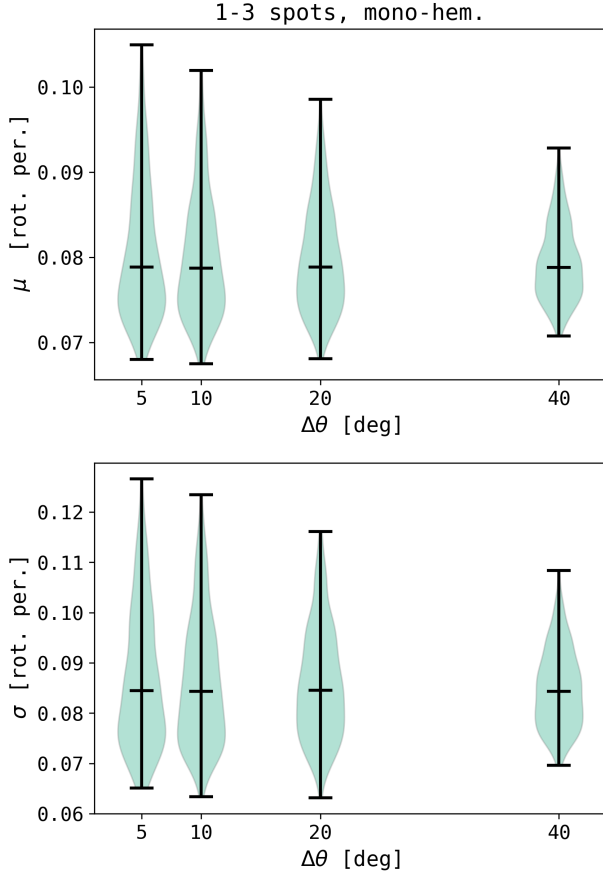
The power law exponent of the flare frequency distribution and the placement of active regions on either one or both hemispheres (like on the Sun) have different effects on the latitude inference: First, a lower power law exponent of the flare frequency distribution by definition decreases the ratio of low to high amplitude flares (see Eq. 1). This increases the number of detected flares close to the limb, where flares are geometrically most foreshortened, by increasing the average energy of flares. Both, the mean waiting time μ and the width of the waiting time distribution σ should slightly decrease as an effect. However, Fig. 8 illustrates that this effect is insignificant in the investigated range of α values. Similarly, since amplitudes closely approximate flare energy (Fig. 2, or, similarly, Hawley et al. 2014), varying flare amplitudes has a small effect on the waiting times, too.

3.4 Realistic light curves are needed for the correct interpretation of flare waiting times

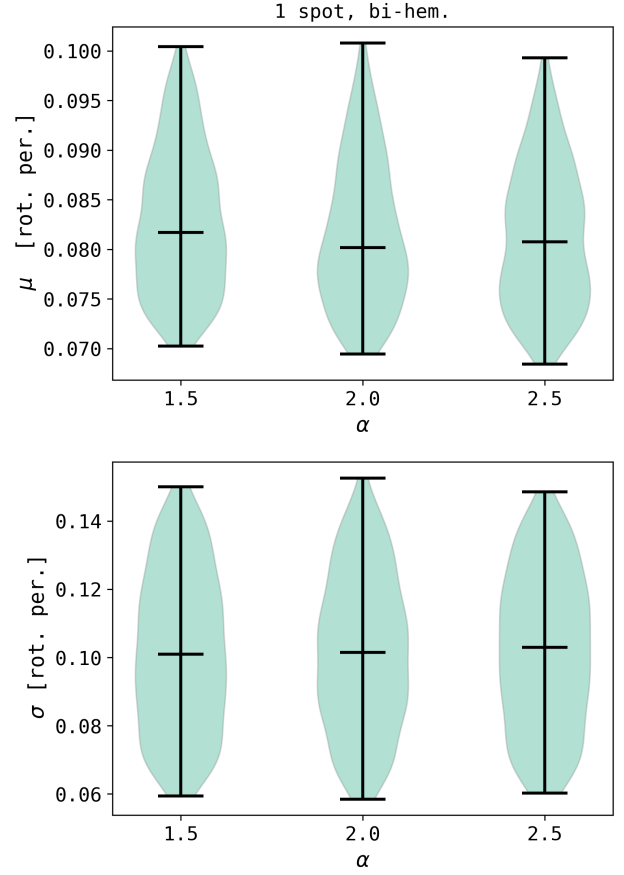
To a first approximation, the trends observed in Fig. 4 are the result of changing night length distributions (Fig. 1) for different active latitudes. At a fixed mean waiting time μ between flares, flaring regions placed at high latitudes would be visible for most orientations of the stellar rotation axis. Only a few regions would be hidden from

Table 2. Best-fit parameters to Eq. 2 for all tested bi- and mono-hemispheric configurations with 1, 1-3, and 3-5 flaring regions (FR).

	1 FR, bi-hem.	1-3 FR, bi-hem.	3-5 FR, bi-hem.	1-3 FR, mono-hem.	3-5 FR, mono-hem.
a_1	-1922 ± 64	-4258 ± 168	-16200 ± 736	-6287 ± 196	-13523 ± 311
a_2	1606 ± 20	3411 ± 60	8536 ± 269	4222 ± 62	7356 ± 111
b_1	577 ± 95	390 ± 325	9997 ± 922	911 ± 327	9425 ± 456
b_2	-1623 ± 25	-3023 ± 80	-7674 ± 273	-3564 ± 73	-6957 ± 121
c	84 ± 1	65 ± 2	16 ± 3	47 ± 1	14 ± 1


Figure 7. Distribution of mean μ (top panel) and standard deviation σ (bottom panel) of waiting time distributions for four groups of simulated 200-star ensembles with varying width of the flaring latitude $\Delta\theta$ (i.e., width of the red strip in Fig. 3). Each group is shown as a blue violin plot with minimum, maximum and median indicated as horizontal black lines. All other parameters are fixed: Each ensemble is composed of stars with 1-3 flaring spots on one hemisphere, and the same average intrinsic flaring rates. For narrow active latitudes, we see wider distributions in μ and σ than for wider active latitudes. This is because narrower active latitudes close to the pole or to the equator produce more extreme waiting time distributions, described by μ and σ , than wider active latitudes.

the observer on average, so that the spread of waiting times σ will be close to a 1-1 relation with μ , as expected from the Poisson process assumption about when flares occur. So in principle, one could hope to find a closed-form solution. However, our method shows that there are observational effects that cannot be integrated in an analytical solution. We run a flare finding algorithm (Ilin 2021) on realistic light curves, where flares are geometrically foreshortened


Figure 8. Same as in Fig. 7, now varying the power law slope α of the flare frequency distribution in an empirically motivated range (see Fig. 13 in Ilin et al. 2021b, for an overview). Each ensemble is composed of stars with a single flaring spot, and the same average intrinsic flaring rates. As opposed to Fig. 7, the waiting time distribution parameters μ and σ (top and bottom panels) are not significantly affected by the changes in α .

with increasing distance from the center of the stellar disk, are cut off at the ends of the light curve, and may randomly overlap. Most importantly, our maximum waiting time is capped at 1 by definition because we measure waiting time in units of rotation period. This, in turn, decreases σ . The combined upshot of these effects is that, almost always, $\sigma \neq \mu$, even in the case of near pole-on active regions (dotted lined in Fig. 4).

3.5 Application to flares on G-type Kepler stars

It is out of the scope of this work to attempt a full-blown analysis of real observations, since that would require 1. careful and extensive sample selection, 2. flare finding and vetting, and 3. rotation period measurements on many stars, including corrections for completeness. However, for smaller samples of stars, analysis that includes several of these steps exists in the literature (Howard et al. 2020a; Tu et al. 2021; Ramsay et al. 2020). We have primarily focused on low-mass, and particularly M dwarfs, in this work (see Fig 2, and the flare model from Davenport et al. 2014). However, the mid-M dwarf flare model is successfully used to describe flares on earlier spectral type stars (Howard & MacGregor 2022; Günther et al. 2020; Jackman et al. 2018), and the ED -amplitude relation is also comparable (Liu et al. 2023). In this Section, we focus on G dwarfs by using results of Okamoto et al. (2021), who searched all G dwarf light curves in the Kepler archive for flares, and determined the stars' rotation periods. Since the Sun, a G dwarf, is the only star for which flaring latitudes are precisely known, a G dwarf ensemble is the only one with a reliable benchmark.

We assume that given the multi-year baseline of Kepler observations for most of the stars in the sample, and the relatively short rotation periods ($P < 40$ d), the rotation phases of all stars are evenly covered by observations. We calculate the rotation phases from the flare times given in the online catalog¹ in Okamoto et al. (2021). We only consider stars with 5-30 detected flares in the data, so that we stay within the limits of our simulations. This mostly removes stars with less than 5 flares, but also some active and bright stars with more than 30 flares, leaving 61 stars in the sample. Then we calculate the mean waiting time μ and standard deviation σ in units of P for the fast ($P < 10$ d) and slow ($P > 10$ d) rotators in the sample. We also further split the fast rotators into very fast ($P < 5$ d), and moderately fast rotators ($5 < P < 10$ d). Within these four subsamples, we may expect that the number of flaring regions and their latitudes will be similar because their dynamos are strongly determined by stellar mass and rotation (Brun & Browning 2017). In particular, around the 10 d mark, stellar activity changes from the saturated regime for fast rotators, where an increase in rotation speed no longer causes an increase in activity, to the unsaturated regime for slow rotators, where rotation and activity are correlated (e.g., in flaring activity, Davenport 2016; Núñez et al. 2022; Ilin et al. 2021b).

In Table 3, we show the numbers of stars and flares in each subsample along with the inferred latitudes using the best-fit values in Table 2 in Eq. 2. Note that the uncertainties on the latitudes are lower limits because our samples are an order of magnitude smaller than those we used to fit the relation in Table 2. We place the μ and σ combination for each subsample in Fig. 9. Given the small sample size, the results have to be interpreted with caution, but we can still make a number of observations.

First, we note that the calculated μ and σ pairs fall into the range of permitted values, suggesting most of the assumptions made for the synthetic data (see Section 2) are consistent with real observations. The likely exception is the assumption that flaring regions are stable throughout the observations (see below). Second, we note that the fast rotator results (red symbols in Fig. 9) indicate similar latitudes in the one-spot case, but for different μ (see also Table 3). Third, the slow rotators appear at even higher μ because they flare less often within a similar observing time as the fast rotators. Overall, they

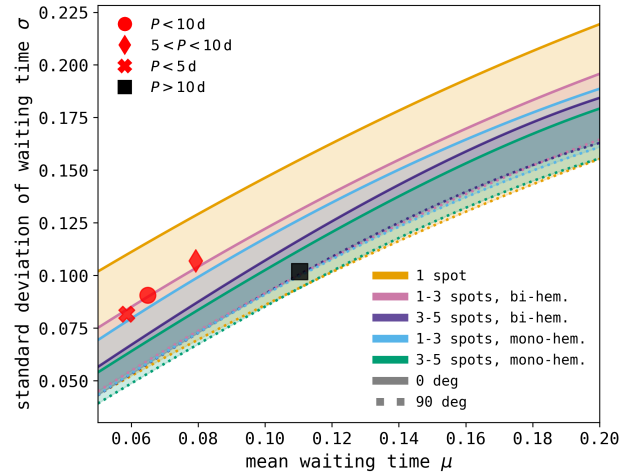


Figure 9. Same as Fig. 4, but with added mean and standard deviation of flaring G dwarfs from Okamoto et al. (2021) in different intervals of the rotation period P (red and black symbols). See Table 3 for the sample parameters and results in each interval.

show a lower spread in waiting times, i.e., they show a lower level of rotational modulation of flare times.

We can interpret the results for fast rotators ($P < 10$ d) in three ways: First, fast rotators only exhibit one active region at mid-latitudes around 45 deg. Second, they only exhibit one active region which appears at a different latitude for each star, because a 45 deg latitude and the flaring-regions-all-over-the-place scenario fall in the same place in Fig. 9. Third, a few (1 to 3) flaring regions may appear at low to mid-latitudes. Alternatively, one active region disappears and another appears at a different longitude, see also the discussion of active region evolution in Section 4.3.

For the slow rotators, we either see a few flaring regions but at very high latitudes, or more than about 3-5 flaring regions in the light curves. We favor the latter option because we expect slowly rotating G dwarfs to have similar flaring activity as the Sun with rather low-latitude flaring regions. Additionally, the lifetime of flaring regions is most likely closer to days or weeks than to the several years of total observations in the Kepler data, which mimics an increased number of active regions in the phase folded waiting times.

Overall, the waiting time distributions favor a relatively small number of active regions (or slow decay of flaring regions) at mid- to low latitudes (or spread all over the surface) for the fast G-type rotators. This is consistent, for instance, with a wide spread of spot latitudes measured by spot occultation on the young Sun-like star Kepler-63 (Netto & Valio 2020), and with the appearance of both high and low latitude spots in fast rotating solar-type stars observed with Doppler Imaging (Strassmeier 2009). In contrast, the data suggest a larger number of flaring regions, or analogously, faster decay for the slow G-type rotators, consistent with photometric time series observations for the Sun and other G dwarfs (McIntosh 1990; Giles et al. 2017). Our results are limited by the unknown active region numbers and lifetimes. This highlights the potential of combining spot measurements and flare timing for determining the distribution of surface magnetic fields on these stars (see Section 4.7).

¹ <https://cdsarc.cds.unistra.fr/viz-bin/cat/J/ApJ/906/72>, retrieved on March 27, 2023.

Table 3. Mean and standard deviation of the flare waiting time distributions for Kepler G-type dwarfs in different rotation periods between P_{min} and P_{max} . Uncertainties on latitudes [in brackets] are lower limits. n_* and n_f are the number of stars and flares in each subsample, respectively. Latitudes for the five different scenarios are inferred using best-fit values in Table 2 with Eq. 2.

	$P < 10$ d	$5 < P < 10$ d	$P < 5$ d	$P > 10$ d
μ	0.065	0.079	0.059	0.11
σ	0.091	0.107	0.082	0.102
n_*	47	18	29	14
n_f	580	176	404	102
P_{min} [d]	0.25	5.03	0.25	10.06
P_{max} [d]	9.77	9.77	4.96	40.04
1 FR, bi. [deg]	38 [3]	32 [3]	43 [3]	78 [4]
1-3 FR, bi. [deg]	-	-	6 [8]	86 [11]
3-5 FR, bi. [deg]	-	-	-	83 [43]
1-3 FR, mon. [deg]	-	-	-	83 [11]
3-5 FR, mon. [deg]	-	-	-	50 [18]

4 DISCUSSION

We have found that we can potentially use the mean and standard deviation of flare waiting times in ensembles of randomly oriented stars to infer the location of active latitudes. Our ensemble technique requires us to define and combine a sample of stars in which we hypothesize the presence of a common active latitude location with a width below ~ 20 deg. Therefore, the method's utility strongly depends on the choice of sample.

A straightforward selection criterion is to choose stars with a similar flaring rate, which is available by definition. In the form of the power law offset β in the stars' flare frequency distribution, it can be used as a proxy of similar small-scale surface field strength and phase of the activity cycle. In analogy to the Solar cycle, we expect that both of these features will vary with the active latitude's location (Hathaway 2015). Further criteria are stellar mass, rotation and age as the basic proxies for the stellar dynamo (Brun & Browning 2017); the number (Section 4.2) and lifetime (Section 4.3) of starspots or active regions; the magnitude of differential rotation (Section 4.4); the current phase of the activity cycle known from activity indicators other than flares (Section 4.5); or the presence of active longitudes (Section 4.6). We note that some, but not all, these criteria were applied in Section 3.5.

In the following, we sometimes use flaring or active regions and spot groups synonymously, but we note that it is not well known how they are spatially related in stars other than the Sun. We sketch out a possible way forward in Section 4.7.

Our method produces active regions that flare following a stationary Poisson process in time, which is well-established on the Sun, but not well known for other stars. We start the discussion by scrutinizing this assumption (Section 4.1).

4.1 Poisson process

Our method assumes that flares occur independently of one another, following a Poisson process within each flaring regions. On the Sun, most flare waiting times are distributed exponentially, consistent with a piece-wise constant Poisson process, with each constant "piece" being 1-3 days long (Moon et al. 2001; Wheatland 2001; Wheatland & Litvinenko 2002). Some flares seem to be causally related, either both in space and time, or mostly in time but not in space, so called "homologous" (e.g., Hanaoka 1996) or "sympathetic" flares (Fritzova-

Svestkova et al. 1976), respectively. The latter are a statistically weak effect compared to the former (Moon et al. 2001; Wheatland & Craig 2006). Sympathetic flares are observed predominantly at low-energies (Wheatland et al. 1998), and in active regions that are less than about 30 deg apart (Pearce & Harrison 1990; Fritzova-Svestkova et al. 1976). For instance, flaring regions that pass the solar disk at the same time have about 12 per cent more flares observed in $H\alpha$ occurring within 10 minutes of one another than independence of events would imply (Wheatland 2006).

It is unclear how far we can extrapolate from solar flares – the largest of which have energies usually below 10^{32} erg – to stellar superflares above 10^{32} erg. Superflares will make up a majority of the observed flares in a stellar ensemble of Sun-like or lower mass stars (Maehara et al. 2012; Davenport 2016; Günther et al. 2020). There is indirect evidence of sympathetic flaring in individual groups of flares in a few very active stars, such as UV Ceti (Panagi & Andrews 1995) and V374 Peg (Vida et al. 2016). In a statistical sense, it is often conjectured that the occurrence of large multip peaked flares, called "complex" flares is due to sympathetic or homologous flaring, because the fraction of such events rises with increasing flare energy (Oskanyan & Terebizh 1971; Davenport et al. 2014; Howard & MacGregor 2022; Hawley et al. 2014; Silverberg et al. 2016). Subsuming multip peaked events into one could at least partially mitigate this deviation from a Poisson process.

Another source of deviation from the Poisson process could be magnetic binary interactions (Salter et al. 2008, 2010), star-planet (Shkolnik et al. 2008; Route 2019) or star-disk (Tsuboi et al. 2000) interactions that trigger reconnection in the stellar corona. There is no solar analog to these phenomena, so that they remain largely unexplored. Binary and star-disk interactions may be taken into account in the sample selection by selecting high-probability single stars, and systems with mostly dissipated disks. Planets around low-mass stars, however, are ubiquitous (Dressing & Charbonneau 2015; Hardegree-Ullman et al. 2019), yet may remain undetected. Magnetic star-planet interaction has only marginally been seen in the timing of flares (Maggio et al. 2015) suggesting a statistically weak effect even in the most active exoplanet hosts known to date, like AU Mic (Ilin & Poppenhaeger 2022). Finally, tidal star planet interactions have been observed to enhance stellar activity level and rotation period (Ilic et al. 2022), and could consequently increase flaring behavior. However, it is not clear how tidal interaction would affect flare timing.

Based on the current evidence, we expect the rotational modulation flare timing to dominate both sympathetic flaring, and flares triggered by interactions with planets. Homologous flares, if they predominantly occur within a short time after a large flare, will be subsumed under one complex event by AltaiPony and most other flare finding algorithms. In practice, one could test the Poisson process assumption using known pole-on flaring stars within the sample, such as AD Leo (Morin et al. 2008; Muheki et al. 2020).

4.2 Number of active regions

Knowing the number of active regions on the stellar surface both helps constrain the state of magnetic field, and directly improves the accuracy of our technique (compare Figs. 5 and 6). The solar dynamo produces bi-hemispheric active latitudes with a median of 5-6 spot groups observed each day, but ranging from none to about 20 daily observed spot groups in the course of the solar cycle (Hoyt

& Schatten 1998a,b). This high number of active regions² would prevent the use of our method if they were distributed randomly at all longitudes. In that case, the waiting time distribution of flares on a solar twin would not contain any information. However, neither are solar active regions distributed randomly in longitude, nor are they all similarly active. About 0.5% of all active regions produce $\sim 40\%$ of all major flares with a preference for one of a few major active longitudes (Bai 1987; Chen et al. 2011). If a small number of extremely active regions produces the majority of large flares on other stars as well, we may only need to consider the largest flares to obtain a clear detection of active latitude.

4.3 Active region lifetimes

Active regions on the Sun produce flares in constant fashion for about 1-3 days between emergence and decay (see Section 4.1). Sunspot groups live between a few days and up to six months, with a median somewhat below two weeks (McIntosh 1990). Starspots have lifetimes up to $\sim 10^2$ d which increase with both later spectral type and spot size (Davenport 2015; Giles et al. 2017; Basri et al. 2022; Namekata et al. 2019) when determined using light curve autocorrelation, and similarly from spot crossings (Močnik et al. 2017). Lifetimes $> 10^3$ d for very young stars are inferred from spot-induced radial velocity variations (Stelzer et al. 2003; Carvalho et al. 2021). On the one hand, the true lifetimes may be even longer because the above measurements are limited by the observing baseline of each star. This would play well with our method because it relies on the presence of a few stable flaring regions on the surface. On the other hand, Basri et al. (2022) point out that the autocorrelation method in particular cannot distinguish between stable spots and dynamic decay and emergence in the same area (as is the case on the Sun, see Bumba & Howard 1965; Sawyer 1968; Castenmiller et al. 1986) that mimic a stationary spot or spot group. However, this is only a problem for our technique if the overall flare rate changes significantly between the decayed and newly emerged regions over the course of a light curve.

4.4 Differential rotation

Differential rotation is a key ingredient in stellar dynamo models (Brun & Browning 2017) that ultimately determines the location of active latitudes. In solar type stars and early M dwarfs, differential rotation can cause rotation periods at different latitudes to vary significantly (Reinhold et al. 2013). For our method, this means that strong differential rotation adds biases to the waiting times that are measured in units of rotation period. However, the problem arises only if the spots that cause the photometric variability, and the flaring regions reside at different latitudes.

If the active latitude is well-constrained within a < 20 deg, and if the photometric variability stems from the same latitudes, the photometric rotation period will be the same as the rotation period of the flaring regions. This is supported by the stability of photometric variability in the presence of differential rotation in young M dwarfs like GJ 1243 (Davenport et al. 2020), and changes in photometric rotation period with stellar cycle (Nielsen et al. 2019).

In rapidly rotating late M dwarfs solar type differential rotation tends to decrease to almost solid body rotation (Barnes et al. 2017), so that the assumption of co-located spots and flares need not be

made. In conclusion, whether differential rotation poses a problem or not hinges upon the spatio-temporal relation of spots and flaring regions.

4.5 Activity cycles

On the Sun, active latitudes shift in a $\sim 20^\circ$ range over the 11-year solar cycle. In an ensemble of flaring stars that are not selected for similar phase in the cycle, this would manifest as widened active regions. Our method tolerates widths up to about 20 deg, but not above (Fig. 7). A very broad active latitude would be seen as converging on the 45 deg bisector of the μ - σ areas in Fig. 4 (see Section 3.2).

Cycles are relatively common among Sun-like (Messina & Guinan 2002; Montet et al. 2017), and, more broadly, GKM stars (Suárez Mascareño et al. 2016), suggesting the presence of solar-like active latitudes. Nielsen et al. (2019) interpret the correlation between the differential rotation rates inferred from spot modulations and the activity cycle phase as evidence for changing active latitude location in 3093 solar-like slow rotating stars observed by Kepler. Lanza et al. (2019) used maximum-entropy spot modeling of the young Sun-like star Kepler-17 to find migration of spot latitudes on a timescale of 400-600 days. Mathur et al. (2014) find that, in the F star KIC 3733735, chromospheric activity correlates with changes in the photometric rotation period. The variability of spot area crossed during exoplanet transits on time scales of multiple years further suggests active latitude-shifting cycles (Estrela & Valio 2016; Zaleski et al. 2020). Particularly, if the photometric variability amplitude remains similar, spots might be migrating out of the transit chord of the planet instead of decaying (Salisbury et al. 2021).

In light of this evidence, choosing an ensemble based on activity cycle phase is advised. A complementary parameter may be rotation rate, since the correlation between direction of the latitude migration and activity switches signs at rotation periods between 10-15 days (Nielsen et al. 2019). If the cycle period is not known, selecting stars with similar flaring rates in the ensemble may circumvent this limitation. The Sun's flaring rate varies from none to over 60 M and X class flares per month over the course of the cycle (Hathaway 2015). Unfortunately, on other stars, evidence for flaring cycles is tentative so far (Muheki et al. 2020; Davenport et al. 2020; Scoggins et al. 2019; He et al. 2018).

4.6 Active longitudes

Although the typical sharp flux peaks of flares stand out in any optical light curve (Davenport et al. 2014; Howard & MacGregor 2022), their optical signature does not give away their longitudes. The amplitude of an individual flare is lower closer to the limb, but is indistinguishable from a flare that naturally happens to have a low amplitude. Our ensemble technique assumes that flaring regions are not only confined to certain latitudes, but also to a low number ≤ 3 of **random** longitudes for the duration of the observation. For multiple active regions, a deviation from randomness may cause complications.

In particular, certain configurations of active longitudes mask the information contained in the flare waiting times. For instance, active longitudes with the same activity levels on opposite sides of the star look the same as high-latitude active regions. This degeneracy breaks when the flaring rates of the two regions are different. The Sun has two active longitudes separated by about 180 deg, and their activity levels flip on timescales of years, with one longitude usually being

² To be doubled to obtain the total number of active regions on the entire solar surface.

slightly dominant (Henney & Harvey 2002; Berdyugina & Usoskin 2003). This flip-flop phenomenon is much more pronounced in other, mostly young, Sun-like stars (Berdyugina 2005).

4.7 Combining spots and flares to infer active latitudes

For flares, latitudinal information is hardly ever available. Only a handful of flares has been directly localized so far (Schmitt & Favata 1999; Wolter et al. 2008; Johnson et al. 2021; Ilin et al. 2021a). A possible solution could be to infer the spatial distribution of spots, and use it to inform the distribution of flaring regions. However, localizing spots systematically is challenging, and the spatio-temporal mapping from spots to flares is everything but precise. We suggest that ensemble studies of both phenomena in tandem could overcome these limitations.

Latitudes and longitudes of starspots Longitudes of magnetic field concentrations can be inferred using optical light curves or spectropolarimetry (Morin et al. 2008, 2010; Namekata et al. 2019; Basri & Shah 2020), and recently, interferometry (Roettenbacher et al. 2022). However, observations of spot crossing events of transiting planets (e.g., Netto & Valio 2020; Silva-Valio et al. 2010) suggest that the resolution of these methods is too low to resolve spot groups, let alone individual spots (Johnstone et al. 2010). Unfortunately, since spot crossings require a frequently transiting planet, ideally in a misaligned orbit, to probe multiple latitudes, there is no systematic, broadly applicable method to resolve spot (groups) on the surfaces of low mass stars.

Spots are even more difficult to localize in latitude than in longitude. Inversions of time resolved spectropolarimetry are usually not unique (Donati & Brown 1997; Kochukhov & Wade 2016; Carroll et al. 2009). Light curves contain latitudinal information only in the presence of differential rotation (Berdyugina 2005). Surface differential rotation can be obtained with the help of ZDI (Morin et al. 2008), using spot migration in longitude (Davenport 2015; Bicz et al. 2022), or asteroseismology (Bazot et al. 2018). Spot crossings of multiple planets (Araújo & Valio 2021), or misaligned ones (Morris et al. 2017; Bazot et al. 2018; Netto & Valio 2020) also resolve the latitudes of spots, although the results are sometimes not fully consistent (Thomas et al. 2019), and the method remains limited to specific star-planet system architectures.

Even if spot localization is coarse at this point, we can still try to find out whether starspots and flares are related similar to the solar case.

Correlations between starspots and flares Keeping in mind the limits of using one-dimensional light curves to infer spot distributions, Shibayama et al. (2013); Maehara et al. (2015, 2017); Notsu et al. (2019); Howard et al. (2020a); Okamoto et al. (2021) observe that the amplitude of spot-induced photometric variability increases with the maximum flare energy in GKM stars, at least compared to the Sun. These results suggest that spot groups that are larger or higher in contrast to the photosphere produce more energetic flares. Recently, Araújo & Valio (2021) reported a more direct correlation between starspot area and flare energy in spot crossing events of Kepler-411 b, albeit no flares were detected during the crossings.

Roettenbacher et al. (2013) found tentative evidence of preferential flaring in phase with rotation for bright flares in a young K-type star. Roettenbacher & Vida (2018) measured a flare preference for occurring in phase with the light curve minimum in a sample of 119 FGKM stars, particularly for the lower energy flares. Howard & Law

(2021) searched for periodicity in flaring times in TESS data, and found that about 1% of late K and M dwarfs have significant period detection in phase with rotation.

In contrast, Doyle et al. (2018, 2019); Feinstein et al. (2020); Ilin & Poppenhaeager (2022); Bicz et al. (2022) do not find correlations between spot phase and flare occurrence in K2 and TESS data of M dwarfs. Doyle et al. (2018) hypothesize that high latitude flaring regions or star-planet interactions could mimic the absence of active longitudes in M dwarfs.

It appears that using spots as a proxy for flaring regions lacks the required precision in both spot localization itself, and in the relations established between the two. Ensemble methods like the one presented in this work could be an alternative way forward for mapping flaring regions and spots – separately, or in tandem.

Combining flare and spot light curve ensemble methods Spots and flares share some observational ambiguities, such as the latitude-inclination degeneracy in spot size and flare amplitude, or the interchangeability of flaring rate and spot size with the number of flaring regions and spots, respectively. Differential rotation, and decay and emergence timescales of individual regions, remain confounding factors for both spot and flare localization techniques from light curves. Luger et al. (2021) have shown that at least the latitude-inclination degeneracy in spots can be overcome using an ensemble approach. In this work, we have shown that the same can be done for flares.

Additionally, some problems that typically trouble spot localization do not bother flares. It is unlikely to mistake one large flare for a combination of smaller ones. Such superpositions occur, but an exact overlap of flares in time is unlikely due to their sharply peaked morphology (see also Section 4.1). Moreover, we cannot choose what spot contributions to include in a light curve inversion. But we can, for instance, place lower limits on the flare energies included in the analysis. In analogy to the Sun, this will constrain the number of flaring regions to the most active ones that are capable of producing the highest energies (Chen et al. 2011). Next, both flares and spots are geometrically foreshortened in white light, so size and temperature contrast are degenerate in a similar way in flares and spots. However, while flare temperatures range between about 7,000 K and > 20,000 K in extreme cases (Howard et al. 2020b; Kowalski et al. 2013; Loyd et al. 2018; Maas et al. 2022), i.e. significantly higher than the photospheres of low mass stars, light curve inversion can be equally successful with bright spots and facular regions, dark spots, or mixtures of both (Basri & Shah 2020). This additional information – clear timing, clear energy separation, and high contrast – will help to tease out the spatial distribution of flares.

Ultimately, combining flare and spot light curve ensemble methods could yield a more complete picture of small scale fields without assuming either as ground truth.

5 SUMMARY AND CONCLUSIONS

In this work, we explore a new technique that uses flare occurrence time in units of stellar rotation period to constrain the number and latitude of flaring regions. We simulated light curves of ensembles of flaring stars with active latitudes with a broad range of properties, such as flare rate and energy distributions, and active latitude width. We found that we could use the mean μ and standard deviation σ of the waiting times between subsequent flares to constrain the active latitude location θ and number of flaring regions of the ensemble stars.

To summarize the technique:

(i) Select a sample of at least 200 stars with supposedly similar active latitudes that flare more than about 5 times each in a continuous light curve.

(ii) Measure the rotation periods of all stars. The light curves should cover at least one full rotation period of the star.

(iii) Phase fold the light curve with the rotation period, and measure the flare peak times in units of rotational phase.

(iv) Calculate μ and σ of the resulting waiting time distribution.

(v) Apply Equation 2 and Table 2 to map μ and σ to latitude given different numbers of flaring regions.

The critical part in this prescription is the choice of sample stars. Flaring region properties of stars other than the Sun are not well constrained. However, proxies such as the flaring rate, age, mass, rotation and spot evolution can be used to pick stars with similar dynamo properties and activity cycle phases that can give rise to active latitudes. Since the relation between starspots and flaring regions is poorly understood, we caution against using spot reconstructions as a proxy for the flaring region distribution. Instead, we argue that ensemble methods for both spots and flares are likely to be complementary, and will be more successful in mapping active latitudes than methods that rely on each phenomenon alone. Since both methods apply to light curves such as obtained by Kepler and TESS, spots and flares already come in tandem. While a full-blown analysis of real observations is out of scope for this work, we apply our technique to a small set of flaring G dwarfs with well-known rotation periods (Okamoto et al. 2021). We find that their waiting time distributions favor more active regions, or equivalently shorter region lifetimes, for slow rotating G dwarfs compared to faster rotating ones, and that accurate latitudes can only be measured when a constraint on the number of spots is available for these stars.

The technique presented here complements recent efforts to characterize small scale magnetic fields by studying the lifetimes and locations of starspots and active regions. Our study aimed to assess the information content of waiting time distributions of currently available flare ensembles, such as from Kepler (Davenport 2016; Yang et al. 2017) and TESS (Günther et al. 2020), which may contain up to a few hundred light curves of stars with similar numbers and latitudes of flaring regions. This currently limits us to using only the lowest order momenta for our analysis. However, with the rapidly growing archives of optical monitoring with TESS, and soon PLATO, the ensemble size may be increased to a thousand or more within the next decade, so that higher order momenta may soon become informative about the distribution of active regions on the surfaces of low mass stars.

ACKNOWLEDGEMENTS

The authors would like to thank Uwe Wolter for numerous constructive suggestions that considerably improved the manuscript. EI would like to thank Sebastian Pineda for providing a sample of ultracool dwarf targets in TESS; and Yuxi (Lucy) Lu, Sam Grunblatt, Isabel Coleman, Joel Zinn, Katja Poppenhäger, Engin Keles, Ward S. Howard, Girish M. Duvvuri, Paul Charbonneau, and Thomas J. Bodgan for helpful discussions. EI acknowledges support from the Fulbright Foundation, and the German Academic Scholarship Foundation.

This project made use of computational systems and network services at the American Museum of Natural History supported by the National Science Foundation via Campus Cyberinfrastructure Grant Awards #1827153 (CC* Networking Infrastructure: High Performance Research Data Infrastructure at the American Museum

of Natural History). This project relies on the open source Python packages `numpy` (Harris et al. 2020), `pandas` (Reback et al. 2022), `matplotlib` (Hunter 2007), and `astropy` (Robitaille et al. 2013).

DATA AVAILABILITY

All modules and scripts required to reproduce the synthetic data, figures, and tables in this study are openly available via GitHub (github.com/ekaterinailin/flare-locations-ensembles-science). The simulation data, Tables 2 and 3 are archived on Zenodo ([doi:10.5281/zenodo.7996929](https://doi.org/10.5281/zenodo.7996929))

REFERENCES

- Airapetian V. S., et al., 2020, *International Journal of Astrobiology*, 19, 136
- Araújo A., Valio A., 2021, *The Astrophysical Journal*, 922, L23
- Bai T., 1987, *The Astrophysical Journal*, 314, 795
- Barnes J. R., Jeffers S. V., Haswell C. A., Jones H. R. A., Shulyak D., Pavlenko Y. V., Jenkins J. S., 2017, *Monthly Notices of the Royal Astronomical Society*, 471, 811
- Basri G., Shah R., 2020, *The Astrophysical Journal*, 901, 14
- Basri G., Streichenberger T., McWard C., Edmond IV L., Tan J., Lee M., Melton T., 2022, *The Astrophysical Journal*, 924, 31
- Bazot M., et al., 2018, *Astronomy and Astrophysics*, 619, L9
- Benz A. O., Güdel M., 2010, *Annual Review of Astronomy and Astrophysics*, 48, 241
- Berdugina S. V., 2005, *Living Reviews in Solar Physics*, 2, 8
- Berdugina S. V., Usoskin I. G., 2003, *Astronomy and Astrophysics*, 405, 1121
- Bice C. P., Toomre J., 2022, *The Astrophysical Journal*, 928, 51
- Bicz K., Falewicz R., Pietras M., Siarkowski M., Preś P., 2022, *The Astrophysical Journal*, 935, 102
- Brown B. P., Oishi J. S., Vasil G. M., Lecoanet D., Burns K. J., 2020, *The Astrophysical Journal*, 902, L3
- Browning M. K., 2008, *The Astrophysical Journal*, 676, 1262
- Brun A. S., Browning M. K., 2017, *Living Reviews in Solar Physics*, 14, 4
- Bumba V., Howard R., 1965, *The Astrophysical Journal*, 141, 1502
- Carroll T. A., Kopf M., Strassmeier K. G., Ilyin I., 2009, *Proc. of Cosmic Magnetic Fields: From Planets, to Stars and Galaxies*, 259, 633
- Carvalho A., Johns-Krull C. M., Prato L., Anderson J., 2021, *The Astrophysical Journal*, 910, 33
- Castenmiller M. J. M., Zwaan C., van der Zalm E. B. J., 1986, *Solar Physics*, 105, 237
- Cauley P. W., Redfield S., Jensen A. G., 2017, *The Astronomical Journal*, 153, 217
- Cauley P. W., Kuckein C., Redfield S., Shkolnik E. L., Denker C., Llama J., Verma M., 2018, *The Astronomical Journal*, 156, 189
- Chadney J. M., Koskinen T. T., Galand M., Unruh Y. C., Sanz-Forcada J., 2017, *Astronomy and Astrophysics*, 608, A75
- Chen A. Q., Wang J. X., Li J. W., Feynman J., Zhang J., 2011, *Astronomy and Astrophysics*, 534, A47
- Chen H., Zhan Z., Youngblood A., Wolf E. T., Feinstein A. D., Horton D. E., 2021, *Nature Astronomy*, 5, 298
- Cheremkov A., Bisikalo D., Fossati L., Möstl C., 2017, *The Astrophysical Journal*, 846, 31
- Davenport J., 2015, PhD thesis, [doi:10.5281/zenodo.47231](https://ui.adsabs.harvard.edu/abs/2015PhDT.....177D), <https://ui.adsabs.harvard.edu/abs/2015PhDT.....177D>
- Davenport J. R. A., 2016, *The Astrophysical Journal*, 829, 23
- Davenport J. R. A., et al., 2014, *The Astrophysical Journal*, 797, 122
- Davenport J. R. A., Mendoza G. T., Hawley S. L., 2020, *The Astronomical Journal*, 160, 36
- Donati J.-F., Brown S. F., 1997, *Astronomy and Astrophysics*, v.326, p.1135-1142, 326, 1135
- Doyle L., Ramsay G., Doyle J. G., Wu K., Scullion E., 2018, *Monthly Notices of the Royal Astronomical Society*, 480, 2153

- Doyle L., Ramsay G., Doyle J. G., Wu K., 2019, *Monthly Notices of the Royal Astronomical Society*, 489, 437
- Dressing C. D., Charbonneau D., 2015, *The Astrophysical Journal*, 807, 45
- Ducrot E., et al., 2018, *The Astronomical Journal*, 156, 218
- Estrela R., Valio A., 2016, *The Astrophysical Journal*, 831, 57
- Fan Y., 2009, *Living Reviews in Solar Physics*, 6, 4
- Feinstein A. D., Montet B. T., Ansdell M., Nord B., Bean J. L., Günther M. N., Gully-Santiago M. A., Schlieder J. E., 2020, *The Astronomical Journal*, 160, 219
- Fritzova-Svestkova L., Chase R. C., Svestka Z., 1976, *Solar Physics*, 48, 275
- García R. A., Ballot J., 2019, *Living Reviews in Solar Physics*, 16, 4
- Gershberg R. E., 1972, *Astrophysics and Space Science, Volume 19, Issue 1, pp.75-92*, 19, 75
- Giles H. A. C., Collier Cameron A., Haywood R. D., 2017, *Monthly Notices of the Royal Astronomical Society*, 472, 1618
- Günther M. N., et al., 2020, *The Astrophysical Journal*, 159, 60
- Hanaoka Y., 1996, *Solar Physics*, 165, 275
- Hardegree-Ullman K. K., Cushing M. C., Muirhead P. S., Christiansen J. L., 2019, *The Astronomical Journal*, 158, 75
- Harris C. R., et al., 2020, *Nature*, 585, 357
- Hathaway D. H., 2015, *Living Reviews in Solar Physics*, 12, 4
- Hawley S. L., Davenport J. R. A., Kowalski A. F., Wisniewski J. P., Hebb L., Deitrick R., Hilton E. J., 2014, *The Astrophysical Journal*, 797, 121
- Hazra G., Vidotto A. A., Carolan S., Villarreal D'Angelo C., Manchester W., 2022, *Monthly Notices of the Royal Astronomical Society*, 509, 5858
- He H., Wang H., Zhang M., Mehrabi A., Yan Y., Yun D., 2018, *The Astrophysical Journal Supplement Series*, 236, 7
- Henney C. J., Harvey J. W., 2002, *Solar Physics*, 207, 199
- Howard W. S., Law N. M., 2021, *The Astrophysical Journal*, 920, 42
- Howard W. S., MacGregor M. A., 2022, *The Astrophysical Journal*, 926, 204
- Howard W. S., Corbett H., Law N. M., Ratzloff J. K., Glazier A., Fors O., del Ser D., Haislip J., 2019, *The Astrophysical Journal*, 881, 9
- Howard W. S., et al., 2020a, *The Astrophysical Journal*, 895, 140
- Howard W. S., et al., 2020b, *The Astrophysical Journal*, 902, 115
- Hoyt D. V., Schatten K. H., 1998a, *Solar Physics*, 179, 189
- Hoyt D. V., Schatten K. H., 1998b, *Solar Physics*, 181, 491
- Huber K. F., Wolter U., Czesla S., Schmitt J. H. M. M., Esposito M., Ilyin I., González-Pérez J. N., 2009, *Astronomy and Astrophysics, Volume 501, Issue 2, 2009, pp.715-728*, 501, 715
- Huber K. F., Czesla S., Wolter U., Schmitt J. H. M. M., 2010, *Astronomy and Astrophysics*, 514, A39
- Hunter J. D., 2007, *Computing in Science & Engineering*, 9, 90
- Ilic N., Poppenhaeger K., Hosseini S. M., 2022, *Monthly Notices of the Royal Astronomical Society*, 513, 4380
- Ilin E., 2021, *Journal of Open Source Software*, 6, 2845
- Ilin E., Poppenhaeger K., 2022, *Monthly Notices of the Royal Astronomical Society*, 513, 4579
- Ilin E., et al., 2021a, *Monthly Notices of the Royal Astronomical Society*, 507, 1723
- Ilin E., Schmidt S. J., Poppenhäger K., Davenport J. R. A., Kristiansen M. H., Omohundro M., 2021b, *Astronomy and Astrophysics*, 645, A42
- Jackman J. A. G., et al., 2018, *Monthly Notices of the Royal Astronomical Society*, 477, 4655
- Johnson E. N., et al., 2021, *Astronomy and Astrophysics*, 651, A105
- Johnstone C., Jardine M., Mackay D. H., 2010, *Monthly Notices of the Royal Astronomical Society*, 404, 101
- Khodachenko M. L., et al., 2007, *Astrobiology*, 7, 167
- Koch D. G., et al., 2010, *The Astrophysical Journal*, 713, L79
- Kochukhov O., Wade G. A., 2016, *Astronomy & Astrophysics*, 586, A30
- Kowalski A. F., Hawley S. L., Holtzman J. A., Wisniewski J. P., Hilton E. J., 2010, *The Astrophysical Journal*, 714, L98
- Kowalski A. F., Hawley S. L., Wisniewski J. P., Osten R. A., Hilton E. J., Holtzman J. A., Schmidt S. J., Davenport J. R. A., 2013, *The Astrophysical Journal Supplement Series*, 207, 15
- Käpylä P. J., 2021, *Astronomy and Astrophysics*, 651, A66
- Kovári Z., Oláh K., 2014, *Space Science Reviews*, 186, 457
- Lammer H., et al., 2007, *Astrobiology*, 7, 185
- Lanza A. F., Netto Y., Bonomo A. S., Parviainen H., Valio A., Aigrain S., 2019, *Astronomy and Astrophysics*, 626, A38
- Lecavelier des Etangs A., et al., 2012, *Astronomy and Astrophysics*, 543, L4
- Liu Q., et al., 2023, *arXiv e-prints*
- Lloyd R. O. P., Shkolnik E. L., Schneider A. C., Barman T. S., Meadows V. S., Pagano I., Peacock S., 2018, *The Astrophysical Journal*, 867, 70
- Luger R., Foreman-Mackey D., Hedges C., 2021, *The Astronomical Journal*, 162, 124
- Maas A. J., et al., 2022, *Astronomy and Astrophysics*, in press
- Maehara H., et al., 2012, *Nature*, 485, 478
- Maehara H., Shibayama T., Notsu Y., Notsu S., Honda S., Nogami D., Shibata K., 2015, *Earth, Planets and Space*, 67, 59
- Maehara H., Notsu Y., Notsu S., Namekata K., Honda S., Ishii T. T., Nogami D., Shibata K., 2017, *Publications of the Astronomical Society of Japan*, 69, 41
- Maggio A., et al., 2015, *The Astrophysical Journal*, 811, L2
- Mathur S., et al., 2014, *Astronomy & Astrophysics*, 562, A124
- McCullough P. R., Crouzet N., Deming D., Madhusudhan N., 2014, *The Astrophysical Journal*, 791, 55
- McIntosh P. S., 1990, *Solar Physics*, 125, 251
- Messina S., Guinan E. F., 2002, *Astronomy and Astrophysics*, 393, 225
- Metcalf T. R., Alexander D., Hudson H. S., Longcope D. W., 2003, *The Astrophysical Journal*, 595, 483
- Meunier N., Lagrange A.-M., 2019, *Astronomy and Astrophysics*, 628, A125
- Meunier N., Lagrange A.-M., Cuzacq S., 2019, *Astronomy & Astrophysics*, 632, A81
- Montet B. T., Tovar G., Foreman-Mackey D., 2017, *The Astrophysical Journal*, 851, 116
- Moon Y.-J., Choe G. S., Yun H. S., Park Y. D., 2001, *Journal of Geophysical Research: Space Physics*, 106, 29951
- Morin J., et al., 2008, *Monthly Notices of the Royal Astronomical Society*, 390, 567
- Morin J., Donati J. F., Petit P., Delfosse X., Forveille T., Jardine M. M., 2010, *Monthly Notices of the Royal Astronomical Society*, 407, 2269
- Morris B. M., 2020a, *Journal of Open Source Software*, 5, 2103
- Morris B. M., 2020b, *The Astrophysical Journal*, 893, 67
- Morris B. M., Hebb L., Davenport J. R. A., Rohn G., Hawley S. L., 2017, *The Astrophysical Journal*, 846, 99
- Morris B. M., Agol E., Hebb L., Hawley S. L., 2018a, *The Astronomical Journal*, 156, 91
- Morris B. M., Agol E., Davenport J. R. A., Hawley S. L., 2018b, *The Astrophysical Journal*, 857, 39
- Močnik T., Southworth J., Hellier C., 2017, *Monthly Notices of the Royal Astronomical Society*, 471, 394
- Muheki P., Guenther E. W., Mutabazi T., Jurua E., 2020, *Astronomy and Astrophysics*, 637, A13
- Namekata K., et al., 2019, *The Astrophysical Journal*, 871, 187
- Netto Y., Valio A., 2020, *Astronomy and Astrophysics*, 635, A78
- Nielsen M. B., Gizon L., Cameron R. H., Miesch M., 2019, *Astronomy and Astrophysics*, 622, A85
- Notsu Y., et al., 2013, *The Astrophysical Journal*, 771, 127
- Notsu Y., et al., 2019, *The Astrophysical Journal*, 876, 58
- Núñez A., et al., 2022, *The Astrophysical Journal*, 931, 45
- Okamoto S., Notsu Y., Maehara H., Namekata K., Honda S., Ikuta K., Nogami D., Shibata K., 2021, *The Astrophysical Journal*, 906, 72
- Oskanyan V. S., Terebizh V. Y., 1971, *Astrophysics*, 7, 48
- Panagi P. M., Andrews A. D., 1995, *Monthly Notices of the Royal Astronomical Society*, 277, 423
- Parker E. N., 1955, *The Astrophysical Journal*, 122, 293
- Pearce G., Harrison R. A., 1990, *Astronomy and Astrophysics (ISSN 0004-6361)*, vol. 228, no. 2, Feb. 1990, p. 513-516., 228, 513
- Perugini G. M., et al., 2021, *Monthly Notices of the Royal Astronomical Society*, 508, 3304
- Rackham B. V., Apai D., Giampapa M. S., 2018, *The Astrophysical Journal*, 853, 122
- Raetz S., Stelzer B., Damasso M., Scholz A., 2020, *Astronomy and Astrophysics*, 637, A22

Ramsay G., Doyle J. G., Doyle L., 2020, *Monthly Notices of the Royal Astronomical Society*, 497, 2320

Reback J., et al., 2022, Pandas 1.4.2, doi:10.5281/zenodo.6408044, <https://zenodo.org/record/6408044>

Reinhold T., Reiners A., Basri G., 2013, *Astronomy and Astrophysics*, 560, A4

Ricker G. R., et al., 2015, *Journal of Astronomical Telescopes, Instruments, and Systems*, 1, 014003

Robitaille T. P., et al., 2013, *Astronomy and Astrophysics*, 558, A33

Rodríguez-López C., 2019, *Frontiers in Astronomy and Space Sciences*, 6, 76

Roettenbacher R. M., Vida K., 2018, *The Astrophysical Journal*, 868, 3

Roettenbacher R. M., Monnier J. D., Harmon R. O., Barclay T., Still M., 2013, *The Astrophysical Journal*, 767, 60

Roettenbacher R. M., et al., 2022, *The Astronomical Journal*, 163, 19

Route M., 2019, *The Astrophysical Journal*, 872, 79

Salisbury M. A., Kolb U. C., Norton A. J., Haswell C. A., 2021, *New Astronomy*, 83, 101477

Salter D. M., Hogerheijde M. R., Blake G. A., 2008, *Astronomy and Astrophysics*, 492, L21

Salter D. M., Kospal A., Getman K. V., Hogerheijde M. R., van Kempen T. A., Carpenter J. M., Blake G. A., Wilner D., 2010, *Astronomy & Astrophysics*, 521, A32

Santos A. R. G., Cunha M. S., Avelino P. P., García R. A., Mathur S., 2017, *Astronomy and Astrophysics*, 599, A1

Sawyer C., 1968, *Annual Review of Astronomy and Astrophysics*, 6, 115

Schmitt J. H. M. M., Favata F., 1999, *Nature*, 401, 44

Schuessler M., Solanki S. K., 1992, *Astronomy and Astrophysics*, 264, L13

Scoggins M. T., Davenport J. R. A., Covey K. R., 2019, *Research Notes of the American Astronomical Society*, 3, 137

Shibayama T., et al., 2013, *The Astrophysical Journal Supplement Series*, 209, 5

Shkolnik E., Bohlender D. A., Walker G. A. H., Collier Cameron A., 2008, *The Astrophysical Journal*, 676, 628

Silva-Valio A., Lanza A. F., Alonso R., Barge P., 2010, *Astronomy and Astrophysics*, 510, A25

Silverberg S. M., Kowalski A. F., Davenport J. R. A., Wisniewski J. P., Hawley S. L., Hilton E. J., 2016, *The Astrophysical Journal*, 829, 129

Stelzer B., et al., 2003, *Astronomy and Astrophysics*, 411, 517

Strassmeier K. G., 2009, *The Astronomy and Astrophysics Review*, 17, 251

Suárez Mascareño A., Rebolo R., González Hernández J. I., 2016, *Astronomy and Astrophysics*, 595, A12

Thomas A. E. L., et al., 2019, *Monthly Notices of the Royal Astronomical Society*, 485, 3857

Tilley M. A., Segura A., Meadows V., Hawley S., Davenport J., 2019, *Astrobiology*, 19, 64

Tsuboi Y., Imanishi K., Koyama K., Grosso N., Montmerle T., 2000, *The Astrophysical Journal*, 532, 1089

Tu Z.-L., Yang M., Wang H. F., Wang F. Y., 2021, *The Astrophysical Journal Supplement Series*, 253, 35

Unruh Y. C., Collier Cameron A., Cutispoto G., 1995, *Monthly Notices of the Royal Astronomical Society*, 277, 1145

Van Doorselaere T., Shariati H., Debusscher J., 2017, *The Astrophysical Journal Supplement Series*, 232, 26

Vida K., et al., 2016, *Astronomy and Astrophysics*, 590, A11

Weber M. A., Browning M. K., 2016, *The Astrophysical Journal*, 827, 95

Wheatland M., 2001, *Solar Physics*, 203, 87

Wheatland M. S., 2006, *Solar Physics*, 236, 313

Wheatland M. S., Craig I. J. D., 2006, *Solar Physics*, 238, 73

Wheatland M. S., Litvinenko Y. E., 2002, *Solar Physics*, 211, 255

Wheatland M. S., Sturrock P. A., McTiernan J. M., 1998, *The Astrophysical Journal*, 509, 448

Wolter U., Robrade J., Schmitt J. H. M. M., Ness J. U., 2008, *Astronomy and Astrophysics*, 478, L11

Yadav R. K., Gastine T., Christensen U. R., Reiners A., 2015, *Astronomy and Astrophysics*, 573, A68

Yang H., et al., 2017, *The Astrophysical Journal*, 849, 36

Zaleski S. M., Valio A., Carter B. D., Marsden S. C., 2020, *Monthly Notices of the Royal Astronomical Society*, 492, 5141

APPENDIX A: WAITING TIME DISTRIBUTIONS FOR EACH SETUP

Fig. A1 shows μ and σ for all simulated ensembles in the five setups: 1 flaring region (FR), panel (a); 1-3 FRs on both hemispheres, panel (b); 3-5 FRs on both hemispheres, panel (c); 1-3 FRs on one hemisphere, panel (d); and 3-5 FRs on one hemisphere, panel (e). Panel (f) shows all 10 deg and 80 deg lines in one panel for visual comparison. The further apart the 10, 45 and 80 deg lines are in each setup, the better the recovery of flaring latitude from μ and σ . The uncertainties also decrease towards lower μ , that is higher flaring rate, in each setup. From the data illustrated here, the parametrization of the latitude as a function of μ and σ is derived.

The simulation results in Fig. A1 (a) and (b) are validated in Figs. 5 and 6. From **top to bottom**, the panels in Figs. 5 and 6 use the relation between (μ, σ) and θ derived from the data in Fig. A1 (a) and (b) from **right to left**.

The results for Fig. A1 (d) and (e) are similar, so we don't produce another validation figure for Fig. A1 (d) in the main text. For Fig. A1 (c) and (e), the uncertainties are too large for a useful estimate of the latitude in a 200-star ensemble, i.e., the 10 and 80 deg lines are closer to each other than the spread in similar ensembles (error bars in Fig. A1 (c) and (e) overlap).

We note that Figs. 5 and 6 use the best-fit values in Table 2 that were derived from the data in Fig. A1 to recover the flaring latitude in a separate synthetic data set. So, Fig. A1 uses training data, while Figs. 5 and 6 use validation data.

This paper has been typeset from a \LaTeX file prepared by the author.

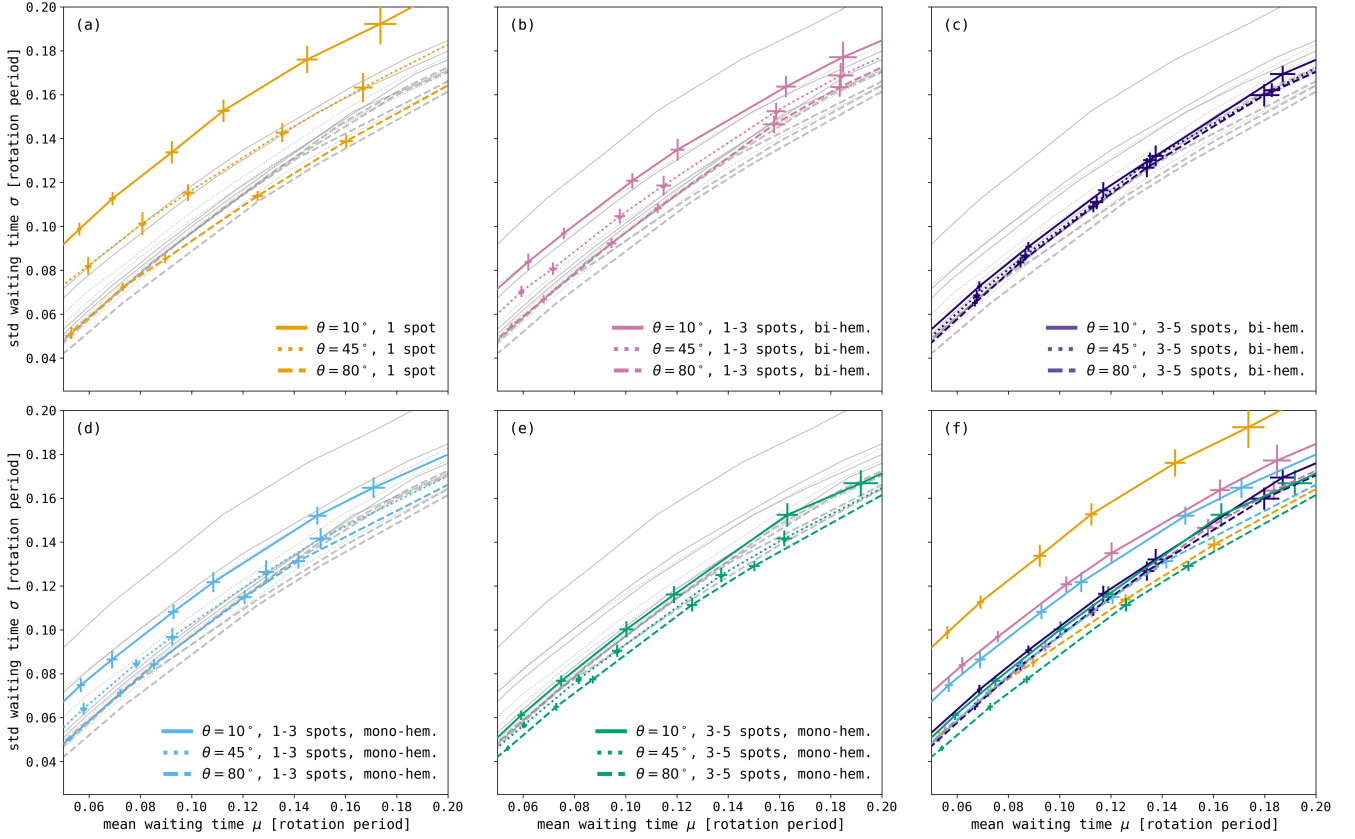


Figure A1. Results for all five investigated simulation setups – 1, 1-3 and 3-5 spots, distributed across either one, or both hemispheres. The gray lines are the same for all panels. They show their combined graphs for visual comparison. Panels (a)-(e) show μ vs. σ , and include the exemplary interpolated lines for 10, 45 and 80 deg, respectively (solid, dotted, and dashed). The uncertainty in each data point is derived using the standard deviation in a group of ensembles in a 3 deg wide latitude bin. Panel (f) overlays the 10 and 80 deg lines from the previous panels.